Utilizing the onset of time-lapse changes: a robust basis for reservoir monitoring and characterization

D. W. Vasco,[1] Thomas M. Daley[1] and Andrey Bakulin[2]

[1]*Lawrence Berkeley National Laboratory, University of California, Berkeley, CA 94720, USA. E-mail: dwvasco@lbl.gov*
[2]*EXPEC Advanced Research Center, Saudi Aramco, Dhahran 31311, Saudi Arabia*

SUMMARY

Time-lapse monitoring is useful for imaging changes in geophysical attributes due to fluid flow. In trying to use time-lapse data for reservoir characterization, difficulties often arise when relating changes in geophysical observations to changes in fluid saturation and pressure. As an alternative approach for reservoir monitoring and characterization, we introduce the idea of an onset time, the time at which a measured quantity, such as a seismic traveltime or a reflection amplitude, begins to deviate from its background value. We illustrate the idea and demonstrate its utility through the consideration of traveltimes recorded by the continuous active source seismic monitoring system at the Frio pilot site near Houston, Texas. The system, which transmits an elastic wave every 15 min, is used to monitor the movement of carbon dioxide injected into a permeable sand formation. From these data we can estimate the onset of changes in seismic traveltimes to six receivers in an adjacent borehole. Numerical simulation and synthetic tests indicate that the onset times are not very sensitive to the method used to compute the effective fluid bulk modulus and, correspondingly, the seismic compressional velocity. Rather, the onset times are strongly influenced by saturation changes within the formation, specifically by the break-through time of the injected fluid phase. By means of an iterative inversion algorithm we use the onset times to estimate permeability variations between the boreholes at the Frio pilot site.

Key words: Inverse theory; Hydrogeophysics; Hydrology; Permeability and porosity; Seismic tomography.

1 INTRODUCTION

We are witnessing an increase in the use of time-lapse geophysical data for the monitoring of fluid flow and for the characterization of flow properties in the subsurface. This increase is observed across a wide range of geophysical subdisciplines. For example, there are a number of techniques from electrical and potential field time-lapse methods that are used to monitor tracer migration, water table movement and the tracking of plumes (LaBrecque & Yang 2001; McKenna *et al.* 2001; Day-Lewis *et al.* 2002; Miller *et al.* 2008; Jardani *et al.* 2009; Doetsch *et al.* 2010a; Martinez-Pagan *et al.* 2010; Karaoulis *et al.* 2011; Coscia *et al.* 2011, 2012). Time-lapse seismic techniques have been used in many contexts, from near surface environmental applications to deeper oil and gas and geothermal reservoirs (Greaves & Fulp 1987; Eastwood *et al.* 1994; Lee *et al.* 1995; Mathisen *et al.* 1995; Watts *et al.* 1996; Lazaratos & Marion 1997; Wang *et al.* 1998; Tura & Lumley 1998; Johnston *et al.* 1998; Burkhart *et al.* 2000; Landro 2001; Smith *et al.* 2001; Behrens *et al.* 2002; Guilbot & Brackin 2002; Arts *et al.* 2004; Osdal *et al.* 2006; Shi *et al.* 2007; Hodgson *et al.* 2007; Daley *et al.* 2007; Daley *et al.* 2008; Chadwick *et al.* 2012; Zhang *et al.* 2012).

Various geodetic data sets, from borehole emplaced tiltmeters to satellite-based techniques such as the global positioning system (GPS) and interferometric synthetic aperture radar (InSAR), have been used to monitor fluid flow associated with environmental remediation, groundwater withdrawal, gas storage and energy production (Evans *et al.* 1982; Palmer 1990; Castillo *et al.* 1997; Fielding *et al.* 1998; Wright 1998; Wright *et al.* 1998; Amelung *et al.* 1999; Mossop & Segall 1999; Vasco *et al.* 2000; Du & Olson 2001; Stancliffe & van der Kooij 2001; Vasco *et al.* 2002; Schmidt & Burgmann 2003; Oppliger *et al.* 2006; Vasco *et al.* 2010; Teatini *et al.* 2011; Rucci *et al.* 2013). Even microseismic activity, associated with the injection of fluids has been used in an effort to track fluid migration (Shapiro *et al.* 1999). Finally, there have been attempts to combine multiple geophysical data sets to infer flow in the subsurface (Hoversten *et al.* 2003).

Recently, there have been several studies extending the use of time-lapse data from simply monitoring fluid flow to subsurface characterization. That is, to use time-lapse geophysical observations to estimate flow properties at depth. The level of sophistication varies from simple assisted history-matching of time-lapse data to the fully coupled inversions of multiple data sets. Initial studies used

time-lapse seismic data to estimate reservoir permeability variations and to identify fast flow paths and barriers to flow (Landa & Horne 1997; Huang *et al.* 1998; He *et al.* 1998; Gosselin *et al.* 2003; Vasco 2004a, Vasco *et al.* 2004; MacBeth & Al-Maskeri 2006; Daley *et al.* 2011). Kowalsky *et al.* (2004, 2006), Camporese *et al.* (2011) and Zhang *et al.* (2014) have used time-lapse electromagnetic data, such as ground penetrating radar and resistivity tomography, to determine flow properties at depth. Geodetic data have also been used for characterization (Vasco *et al.* 2001; Vasco 2004b, Vasco & Ferretti 2005; Rucci *et al.* 2010). Such data are typically very cost-effective, allowing for dense temporal sampling. The variation in microseismicity has been used to infer the hydraulic diffusivity at depth (Shapiro *et al.* 1999; Shapiro *et al.* 2002).

While time-lapse observations have proven useful for reservoir characterization, a fundamental challenge remains. The difficulty is in specifying the relationship between saturation and pressure changes within a reservoir and variations in geophysical properties such as seismic velocity, electrical conductivity and volume strain. Consider the relationship between seismic compressional velocity and fluid saturation changes. It is well known that this relationship is complicated by a host of factors, such as the spatial variation of rock properties and/or fluid distribution at a scale larger then a core sample but smaller then a seismic wavelength, the mesoscopic scale (White 1975; Pride *et al.* 2004). Determining the mesoscopic variations in rock properties and fluid saturations in a reliable fashion is an extremely difficult task. Thus, such information is unlikely to be available for most characterization efforts. Furthermore, there are other factors that can confound the situation, such as physical and chemical changes within the rock caused by the invading fluid (Ghosh & Sen 2012). Such factors can be time-dependent and are not currently well understood. Given the significant variability in rock types within the Earth, it may prove difficult to develop a sufficiently general model with properties that can be reliably determined by geophysical observations.

Here, we take a different approach, based upon the idea of an onset time. An onset time is that point in time at which a geophysical property begins to deviate from its background, or initial, value. The estimation of onset times requires sufficient temporal sampling to capture the initiation of a change in a geophysical observation. In many situations, the onset time can be related to saturation and/or pressure changes within the reservoir. In the example presented below, onset times are associated with the arrival of injected carbon dioxide at various locations in the subsurface. Rather than invert the seismic traveltime changes themselves, we invert the onset time of the changes. Such an approach removes the requirement that we map a change in a geophysical property to a specific change in fluid saturation and/or pressure. Rather, we must relate the initiation of a change in the geophysical property to the arrival time of a saturation front and/or the time at which the fluid pressure changes most rapidly. Such fluid phase arrival times can often be linked to flow properties. For example, as shown in Vasco & Datta-Gupta (1999) and Vasco & Finsterle (2004), tracer arrival times have a rather direct relationship to spatial variations in permeability. Similarly, it was noted in Vasco *et al.* (2000) the arrival time of the largest fluid pressure change has a much simpler relationship to flow properties then does the magnitude of the fluid pressure changes. Due to the non-linearity associated with multiphase flow, the arrival time of a saturation change is somewhat more complicated. In a series of papers (Vasco *et al.* 1999; Vasco & Datta-Gupta 2001; Vasco *et al.* 2004; Vasco 2011) have shown that the saturation arrival time has a direct relationship to reservoir flow properties.

This work follows on from two previous studies in which geodetic data were used to infer the propagation of volume change within a reservoir (Vasco 2004b, Rucci *et al.* 2010). Vasco (2004b) demonstrated that the onset of the most rapidly variation in reservoir volume was directly related to the spatial variation of the flow properties within the reservoir. Rucci *et al.* (2010) indicated that this relationship was not sensitive to the spatial variations of geomechanical properties within the reservoir. The theoretical result was verified in an application to InSAR data from a carbon capture and storage project at In Salah, Algeria. In this paper, we formalize the approach, based upon the notion of an onset time given above, and illustrate its application to a time-lapse crosswell seismic data set. As in the geodetic applications, we find that a collection of onset times, derived from the crosswell data, provide a robust data set with which we may infer flow properties. In particular, the relationship between onset times and flow properties, is not sensitive to the rock physics model. One may take advantage of this characteristic in a wide array of applications.

2 METHODOLOGY

In this section, we relate the onset time to the flow properties of the porous medium, such as the porosity or permeability. As a specific illustration, we consider seismic time-lapse monitoring of carbon dioxide injected into a heterogeneous reservoir. In truth, the methodology is applicable to any time-lapse data set with a temporal sampling that is dense enough to capture the onset of a change in a geophysical attribute.

2.1 Modelling flow: relating saturation changes to the flow properties of the porous medium

2.1.1 *Governing equations for saturation and pressure changes*

Consider a porous medium containing two fluid phases. We denote the saturation of the aqueous phase by $S_w(\mathbf{x}, t)$, while the saturation of the non-aqueous phase is represented by $S_n(\mathbf{x}, t)$. Both saturations vary as functions of the spatial $\mathbf{x}$ and temporal t coordinates. Since the pore space is completely filled by the fluids, the saturations must satisfy the relationship

$$S_w + S_n = 1. \tag{1}$$

The pressure associated with each fluid within the pore space may differ, introducing surface tension on the interface between the fluids and causing one fluid to impinge upon the other. This difference, the capillary pressure (p_c), is given by

$$p_c = p_n - p_w, \tag{2}$$

where p_n is the pressure in the non-wetting or non-aqueous phase and p_w is the pressure in the wetting phase. It is generally assumed, based upon empirical evidence provided by laboratory experiments, that the capillary pressure is a function of the saturation (Peaceman 1977, p. 14):

$$p_n - p_w = p_c(S_w). \tag{3}$$

Fluid velocities are given by two-phase generalizations of Darcy's law, which states that the velocities for the aqueous and non-aqueous phases are driven by their respective pressure gradients and gravitational forces

$$\mathbf{v}_w = -\frac{K k_{rw}}{\phi \mu_w} \left(\nabla p_w - \rho_w g \mathbf{Z} \right), \tag{4}$$

$$\mathbf{v}_n = -\frac{K k_{rn}}{\phi \mu_n} \left(\nabla p_n - \rho_n g \mathbf{Z} \right), \tag{5}$$

where $K(\mathbf{x})$ is the absolute permeability which depends upon spatial position $\mathbf{x}$ but not upon the time, $\phi(\mathbf{x})$ is the porosity, μ_w and μ_n are the fluid viscosities, ρ_w and ρ_n are the fluid densities, g is the gravitational acceleration, $\mathbf{Z}$ is a unit vector in the direction of the gravitational field and $k_{rw}(S_w)$ and $k_{rn}(S_w)$ are the relative permeabilities, given by the ratio of the effective permeability of each fluid to the absolute permeability K (Peaceman 1977, p. 15):

$$k_{rw}(S_w) = \frac{K_w}{K} \le 1, \tag{6}$$

$$k_{rn}(S_w) = \frac{K_n}{K} \le 1. \tag{7}$$

By combining the equations for the conservation of each phase and the two-phase generalization of Darcy's law, one may derive the coupled equations governing two-phase flow in a heterogeneous porous medium (Peaceman 1977, p. 16):

$$\nabla \cdot \left[\frac{\rho_n K k_{rn}}{\mu_n} \left(\nabla p_n - \rho_n g \mathbf{Z} \right) \right] + q_n = \frac{\partial \left(\phi \rho_n S_n \right)}{\partial t}, \tag{8}$$

$$\nabla \cdot \left[\frac{\rho_w K k_{rw}}{\mu_w} \left(\nabla p_w - \rho_w g \mathbf{Z} \right) \right] + q_w = \frac{\partial \left(\phi \rho_w S_w \right)}{\partial t}, \tag{9}$$

where q_n and q_w are the source or sink terms for the respective phases. Eqs (8) and (9), being non-linear and containing spatially varying coefficients, are typically solved numerically. Here, we use the numerical reservoir simulator TOUGH2 (Pruess *et al.* 1999; Pruess 2004) to solve the coupled system of eqs (8) and (9) for a particular reservoir model and specific boundary conditions. For our synthetic application we simulated the injection of carbon dioxide into a 2.5-m thick layer. Variably-sized grid blocks are used to capture the rapid changes in fluid saturations and pressures near the wells (Fig. 1). A heterogeneous permeability model was generated by spatially smoothing a random field (Fig. 2).
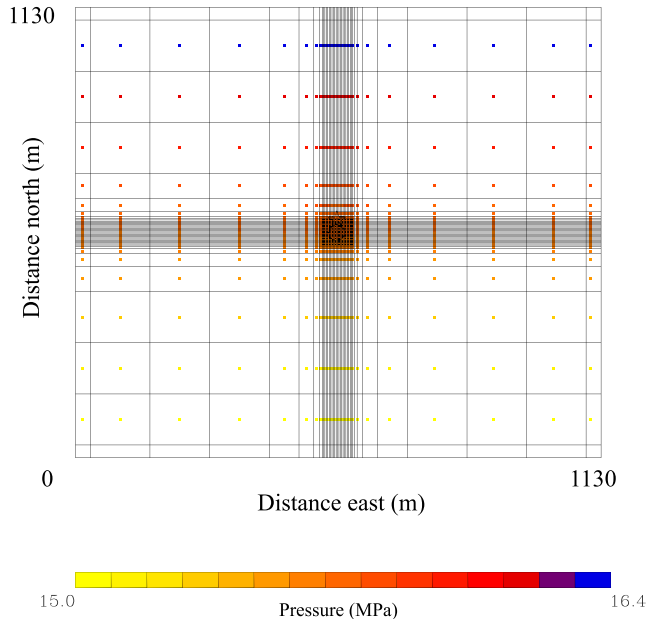
Figure 1. Geometry of the grid used in the numerical simulation of the injection of carbon dioxide at the Frio pilot site. Pressure variations are indicated by the small coloured squares at the center of each grid block.
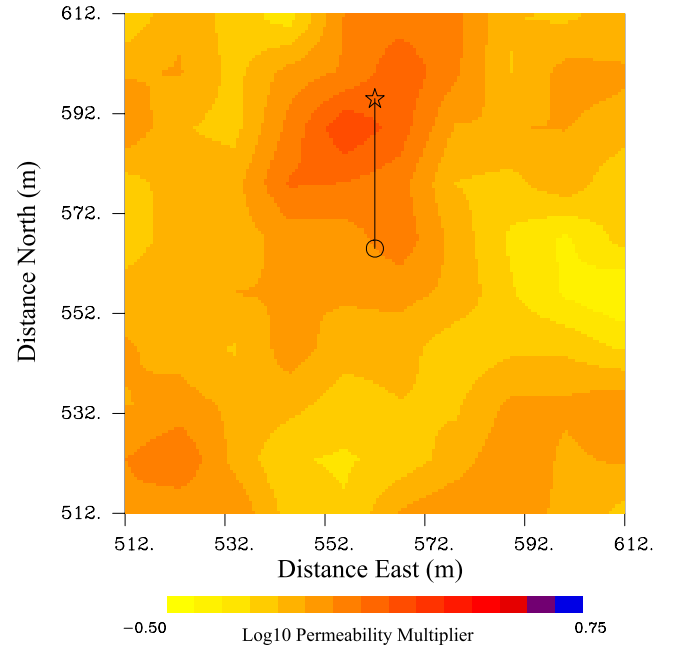
Figure 2. Reference permeability model used to generate synthetic travel-time changes induced by the injection of carbon dioxide into a central well, denoted by the unfilled circle. The variations in tone denote changes in the logarithm of permeability. The monitoring well in indicated by the unfilled star 30 m to the north of the injector. The straight line connecting the two wells signifies the intersection of a crosswell plane with the reservoir layer.

2.1.2 An equation for saturation arrival times

By solving the governing equations numerically we can derive saturation and pressure histories for each grid block in our reservoir model. We can construct the saturation arrival time from these histories and the corresponding propagation time from the injection well to each grid block. In this way, results from the numerical simulation can be used to construct a path $\mathbf{X}(\mathbf{x}_o, t)$, specified by the observation point $\mathbf{x}_o$ and the time t, extending from the injector to the observation point. One simply follows the saturation evolution backward in time, starting from the arrival time at a given observation point back to the beginning of injection at the well. At any point along that path the instantaneous velocities of the phases are given by eqs (4) and (5). From the path $\mathbf{X}$ and the instantaneous fluid phase velocities we can calculate the arrival time of the injected fluid and the traveltime along the path. For example, in the case of the non-aqueous phase, the traveltime is given by

$$\tau = \int_{\mathbf{X}} \frac{dr}{|\mathbf{v}_n|} \tag{10}$$

or, using eq. (5),

$$\tau = \int_{\mathbf{X}} \frac{\phi \mu_n}{K k_{rn} |\mathbf{U}_n|} dr \tag{11}$$

where

$$\mathbf{U}_n = \nabla p_n - \rho_n g \mathbf{Z}. \tag{12}$$

Expression (11) provides a relationship between the arrival time of the non-aqueous phase and the flow properties of the porous medium. As such, it will serve as the basis of our inversion algorithm. Note that the velocity vector $\mathbf{v}_n$ contains both an explicit and an implicit dependence upon the permeability. The implicit dependence follows from the fact that the expression for $\mathbf{U}_n$ contains the pressure gradient ∇p_n which is a function of the permeability

distribution within the reservoir. As noted in the Appendix [eq. (A10), also see eqs (1–57) in Peaceman (1977)], the velocity vector $\mathbf{v}_n$ also depends upon the fractional flow properties of the two fluids and the capillary pressure curve. For brevity, we shall not discuss this in further detail. We will assume that the overall relative permeability and capillary pressure properties of the formations are characterized by laboratory experiments. Furthermore, we shall recompute the vector $\mathbf{v}_n$ at each iteration of our inversion algorithm when we compute the sensitivities.

2.1.3 Sensitivities: relating perturbations in permeability to perturbations in saturation arrival times

For our iterative inversion algorithm we adopt the general approach described in Vasco *et al.* (2004), in which reservoir permeabilities are updated in order to match the onset times. We begin our derivation by writing the integrand in eqs (10) and (11) as

$$I(r, t) = \frac{1}{|\mathbf{v}_n|} = \frac{\phi \mu_n}{K k_{rn} |\mathbf{U}_n|}, \tag{13}$$

where we have included a dependence upon t because the vector field $\mathbf{v}_n$ can change with time, particularly if there is a change in injection or production. A perturbation in the integrand due to a change in the model parameters leads to a perturbation in the arrival times according to:

$$\delta\tau = \int_{\mathbf{X}} \delta I(r, t)\, dr. \tag{14}$$

The perturbation in flow properties will generally change the flow field and hence the integration path $\mathbf{X}$. As in geophysical tomographic algorithms, we have ignored this effect and integrated along the path computed using the background reservoir model.

Assuming that the fluid, the relative permeability and the capillary pressure properties are fixed, perturbations may occur in the porosity, the permeability, and because of its implicit dependence on porosity and permeability, the velocity vector $\mathbf{U}_n$ may also undergo a perturbation. A general perturbation in $I(r, t)$ may therefore contain the following contributions:

$$\delta I(r, t) = \frac{\partial I}{\partial \phi}\delta\phi + \frac{\partial I}{\partial K}\delta K + \frac{\partial I}{\partial |\mathbf{U}_n|}\delta|\mathbf{U}_n|. \tag{15}$$

The partial derivatives are obtained from the analytic form for $I(r, t)$, eq. (13). As in Vasco *et al.* (2004), we shall neglect the implicit sensitivity of $\mathbf{U}_n$ to changes in the porosities and permeabilities in a single grid block of the reservoir model. In computing sensitivities to a change in a single grid block, we shall assume that the effect of a perturbation to the flow field, $\mathbf{v}_n$, does not change the perturbation in the saturation traveltime. Numerical tests in Vasco & Datta-Gupta (2001) and Vasco *et al.* (2004) indicate that this is an adequate approximation. Thus, we neglect the term associated with perturbation in $\delta|\mathbf{U}_n|$.

Vasco *et al.* (1999, 2004) noted the tradeoff between changes in porosity and changes in permeability. That is, the porosity sensitivity is the negative image of the permeability sensitivity:

$$\frac{\partial I}{\partial \phi} = -\frac{\partial I}{\partial K}$$

and one may write eq. (15) as

$$\delta I(r, t) = \frac{\partial I}{\partial K}(\delta K - \delta\phi) = \frac{\partial I}{\partial K}\delta K',$$

where we have neglected the $\delta|\mathbf{U}_n|$ term, as noted above. Therefore, it is not possible to resolve these parameters independently using

onset times and we must solve for an effective permeability change, $\delta K' = \delta K - \delta\phi$. From this point on we shall drop the prime and treat this quantity as the effective permeability of the medium. It might be possible to incorporate other types of data to resolve this trade-off. Under these restrictions, eq. (14) takes the form

$$\delta\tau = -\int_{\mathbf{X}} I \frac{\delta K}{K}\, dr = -\int_{\mathbf{X}} \frac{1}{|\mathbf{v}_n|}\frac{\delta K}{K}\, dr. \tag{16}$$

An alternative is to simply solve for the ratio ϕ/K, which is better constrained by the onset time data.

2.2 Relating changes in seismic arrival times to saturation changes and onset times

Our observations will be seismic traveltimes for elastic waves generated by a source in one borehole and recorded by a set of hydrophones in an adjacent borehole, as described in Daley *et al.* (2011). The overall set-up (Fig. 3) consists of a single source in the injection well. The source is situated somewhat above the injection interval and activated every 15 min. The transmitted elastic waves are recorded in six borehole receivers in the observation well. The background elastic velocity structure was derived from a sonic log in the injection well at the actual Frio site. The boundaries of the reservoir layer, which is 2.5 m thick and dips 18°, are indicated by the two solid lines in Fig. 3.

Currently, theories relating changes in fluid saturation to changes in the propagation velocity of elastic waves in a porous medium
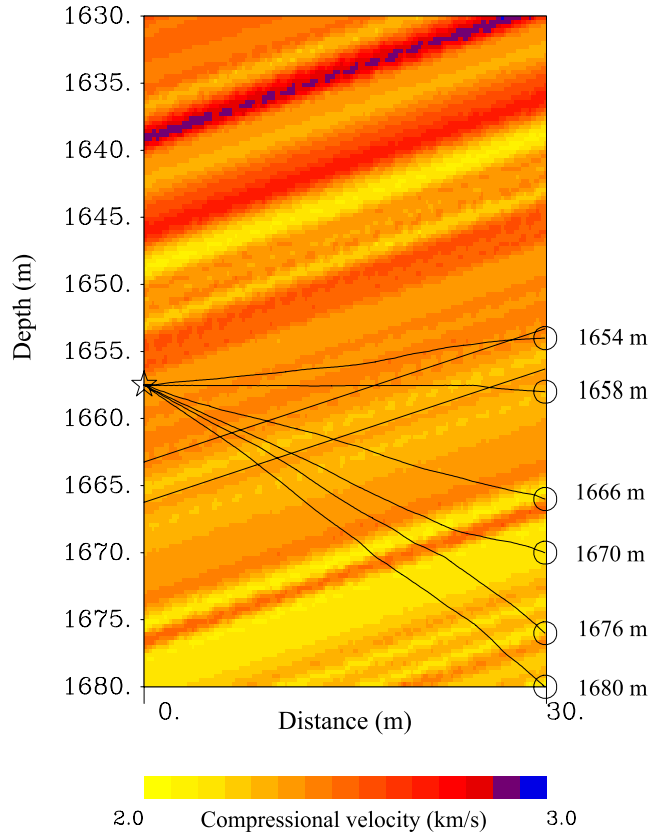
Figure 3. Compressional wave velocity variations between the injection (left edge) and observation (right edge) boreholes. The unfilled star indicates the location of the seismic source. The open circles denote the locations of the labelled receivers. Seismic raypaths are indicated by the trajectories connecting the source to the receivers.

are active areas of research (Müller *et al.* 2010). It appears that the relationship between a variation in fluid saturation and a change in elastic velocity depends upon the distribution of the fluids within the pore space at a scale smaller then that of the seismic wavelength (White 1975; Johnson 2001). In order to explain the variation in seismic wave speed and attenuation as a function of frequency, it is necessary to invoke variations in medium properties or fluid saturations on a length scale smaller then the seismic wavelength and larger then the pore scale, the so-called mesoscopic scale. In this model, the heterogeneity necessitates fluid pressure equilibration over a time interval that is related to the spatial length-scale and the variations in properties. This notion, recently advocated by Pride *et al.* (2004) in a generalization of earlier studies, has been elaborated and utilized by others. For an overview of many related contributions, see the review by Müller *et al.* (2010). The implication of this mesoscale structural dependence on estimates of onset times is not altogether clear and is explored next. Specifically, in the next subsection we consider upper and lower bounds on seismic velocity changes. Following that, we examine how estimates of onset times vary as these bounds are attained.

2.2.1 Relating changes in fluid saturation to changes in seismic velocity

The specific upper and lower limits that we shall consider are the classic Voigt and Reuss bounds (Mavko *et al.* 1998). The Voigt upper bound for the bulk moduli of a mixture of N fluids is given by

$$K_v(\mathbf{x}, t; \tau) = \sum_{i=1}^{N} S_i(\mathbf{x}, t; \tau) K_i, \tag{17}$$

where $S_i(\mathbf{x}, t; \tau)$ is the saturation of the ith fluid and K_i is the bulk modulus of the ith fluid. We use a notation in which the dependence upon the arrival time of the saturation change, τ, given by eq. (10), is explicit. That is, the saturation begins to change when t exceeds τ at a particular location. The magnitude of the saturation change from that time on depends upon $t - \tau$. The Voigt upper bound is obtained when all the contributing components are arranged in parallel. One can visualize this as layers of pure components arranged parallel to the direction of compression. Then the stiffest layer determines the compressibility and controls the modulus. The Reuss lower bound for the effective fluid bulk modulus is given by

$$K_r(\mathbf{x}, t; \tau) = \left[\sum_{i=1}^{N} \frac{S_i(\mathbf{x}, t; \tau)}{K_i} \right]^{-1}. \tag{18}$$

This lower bound is obtained when all the components are arranged in series. The Reuss bound can be thought of as compression in a direction perpendicular to layers of pure components. Thus, the weakest layer plays a significant role in the compressibility of the stack of layers and, to a large degree, determines the modulus. The Hill average fluid bulk modulus (Hill 1963) is simply the average of the Voigt and Reuss Bounds:

$$K_h(\mathbf{x}, t; \tau) = \frac{K_v + K_r}{2}. \tag{19}$$

Bounds such as these are used in a variety of physical settings, as in thermal conductivity where they are known as the Wiener bounds (Wiener 1910; Tong *et al.* 2009). Other bounds, such as the Hashin-Shtrikman bounds (Hashin & Shtrikman 1963), are possible but the Voigt-Reuss bounds are the simplest and the most conservative for a particular volumetric mixture of fluids. For example, the

Voigt-Reuss bounds are valid in the presence of anisotropy while the Hashin-Shtrikman bounds are only valid for a macroscopically homogeneous and isotropic material.

The effective bulk modulus of the entire saturated rock, K_s, including the two fluids (water and carbon dioxide), the properties of the rock constituents or grains, and the frame moduli is given by Gassmanns (1951) relation

$$K_s(\mathbf{x}, t; \tau) = K_d + \frac{(1 - K_d/K_g)^2}{\phi/K_f(\mathbf{x}, t; \tau) + (1 - \phi)/K_g + K_d/K_g^2}, \tag{20}$$

where K_d is the dry frame bulk modulus, K_g is the bulk modulus of the solid grains comprising the rock, K_f is the fluid bulk modulus given by the Voigt (17), Reuss (18), or Hill (19) prescriptions. The density of the saturated rock is given by

$$\rho_s(\mathbf{x}, t; \tau) = \phi \rho_f(\mathbf{x}, t; \tau) + (1 - \phi) \rho_g \tag{21}$$

where

$$\rho_f(\mathbf{x}, t; \tau) = \sum_{i=1}^{N} S_i(\mathbf{x}, t; \tau) \rho_i, \tag{22}$$

and ρ_i is the density of the ith fluid under reservoir conditions. We assume that the shear modulus is not strongly influenced by the presence of the fluids and may be approximated by the shear modulus of the unsaturated rock, G_d. The seismic compressional velocity, V_p, is given by the expression

$$V_p(\mathbf{x}, t; \tau) = \sqrt{\frac{K_s(\mathbf{x}, t; \tau) + \frac{4}{3} G_d}{\rho_s(\mathbf{x}, t; \tau)}} \tag{23}$$

for a given saturation. The Voigt-Reuss velocity bounds are plotted in Fig. 4 as functions of the saturation of carbon dioxide, along with the estimates of Hill (1963). These bounds were computed using the properties associated with the Frio sandstone formation and the pressure and temperature conditions of the reservoir. The difference between the upper and lower velocity values is significant, of the order of the entire velocity variation due to changes in the fluid saturation. Such large differences highlight the importance of the
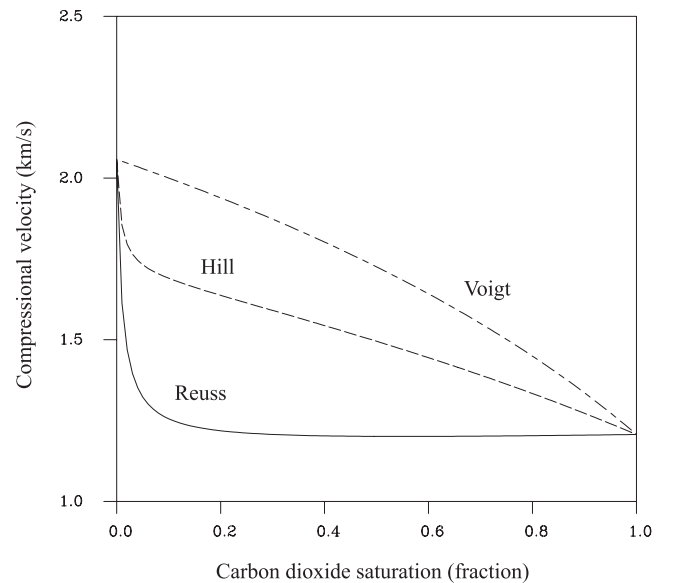
Figure 4. Velocity bounds computed using the Voigt [eq. (17)] and Reuss [eq. (18)] algorithms. The Hill velocity estimate, which is the average of the two bounds [eq. (19)] is also plotted as a function of the carbon dioxide saturation.

rock physics model when interpreting the magnitude of seismic velocity and amplitude changes (Mavko *et al.* 1998).

2.2.2 Computing seismic traveltimes

The basic observations are seismic traveltimes, $T(\mathbf{x}, t; \tau)$, the times required for the propagation of an elastic wave from the source to a set of hydrophones in the observation well. Given a velocity model $V_p(\mathbf{x}, t; \tau)$, high-frequency seismic first arrival times are calculated by solving the Eikonal eq. (Chapman 2004, p. 139)

$$\nabla T \cdot \nabla T = \frac{1}{V_p^2(\mathbf{x}, t; \tau)}. \tag{24}$$

The surface

$$T(\mathbf{x}, t; \tau) = C \tag{25}$$

for some constant C defines a wave front, a surface of constant seismic traveltime from the source. As indicated in Chapman (2004, p. 139) one can consider a ray path $\mathbf{R}(s)$, the trajectory orthogonal to the wave fronts, where s is the distance along the path. In coordinates oriented along the ray, the eikonal equation reduces to

$$\frac{\mathrm{d}T}{\mathrm{d}s} = \frac{1}{V_p(\mathbf{x}, t; \tau)}. \tag{26}$$

By integrating (26) along the ray path we arrive at an expression for the traveltime of a compressional elastic wave

$$T(\mathbf{x}, t; \tau) = \int_{\mathbf{R}} \frac{\mathrm{d}s}{V_p(\mathbf{x}, t; \tau)}. \tag{27}$$

This expression provides a mapping between saturations and seismic traveltimes. We can use it to relate the arrival of the injected fluid phase at points along the ray path to the onset of changes in the traveltime of the seismic wave. The onset time for a particular receiver is due to saturation changes encountered by the segment of the ray path within the reservoir. When the saturation front crosses

the ray path, the velocity is lowered and the traveltime increases. Note that if the saturation change were associated with an increase in velocity then it may be possible for the ray path to shift before the fluid front arrives. For the injection of carbon dioxide the velocity will decrease and the ray will tend to bend around the zone of lower velocity. Our modelling indicates that the shifting of the ray paths is generally not significant up to the onset time, and it is acceptable to use the background velocity model to compute the rays up to the onset time.

2.2.3 The influence of the effective fluid bulk modulus on the calculated traveltime changes and onset times

As an illustration, consider the crosswell geometry shown in Fig. 5. The dipping layered velocity structure (Fig. 3) serves as the background model. Saturation changes lead to velocity decreases within the reservoir layer, as indicated by the panel on the right. The magnitude of the velocity decrease, calculated using Hill's method, 0.5 km s^{-1}, agree with the P-velocity changes seen in the Frio-I pilot time-lapse crosswell experiment (Daley *et al.* 2008). To compute the ray paths we solve the Eikonal eq. (24) numerically using a finite-difference algorithm as proposed by Vidale (1988) and implemented by Podvin & LeComte (1991). The resulting traveltime fronts, corresponding to 5 d of injection, are shown in the left-hand panel of Fig. 5. The seismic ray paths are obtained using an iterative technique to march down the gradient of the travel field from the receivers in the direction of decreasing traveltime. The important component of the ray path is that part intersecting the reservoir layer. The first encounter with a saturation change will lead to the onset of a change in the arrival time of the seismic wave at the receiver. We define the onset time as the calendar time at which the traveltime change exceeds 10 per cent of the peak change. This value is arbitrary but is thought to represent a reasonable noise level associated with time-lapse estimates. The exact value used in applications will
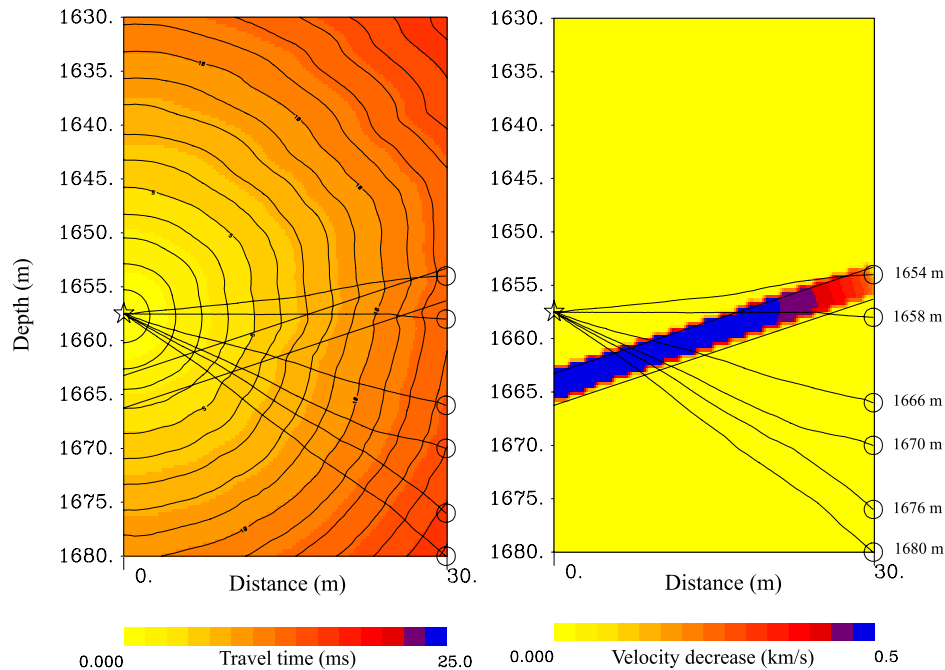
Figure 5. (Left) Contours of traveltime for an elastic wave generated at the source (unfilled star). The contour interval is 1 ms in this plot. The background velocity model for the traveltime computations is plotted in Fig. 3. (Right) Velocity deviations from the background velocity model due to the injection of carbon dioxide into the reservoir layer. The raypaths are indicated by the trajectories from the seismic source to the six receiver locations (open circles).
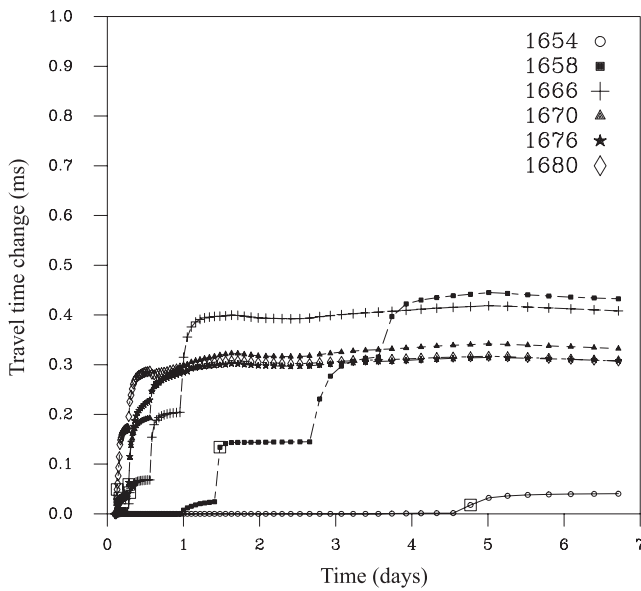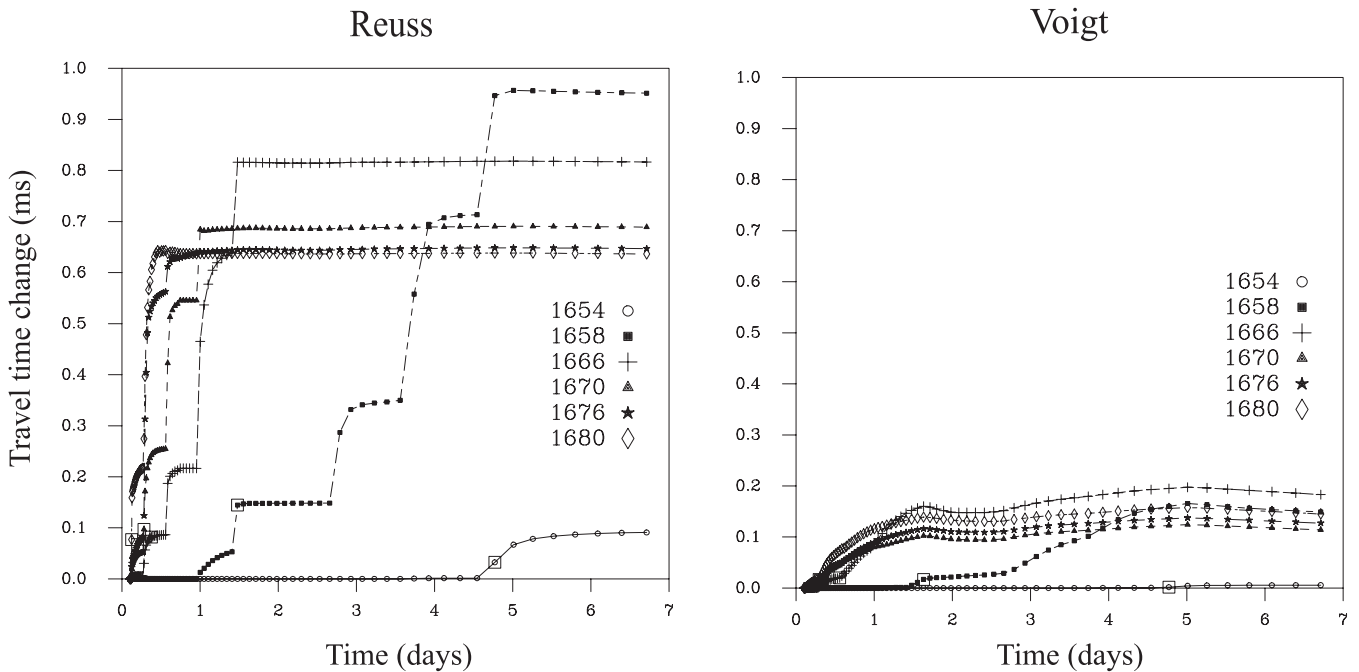
Figure 6. Deviations from pre-injection traveltimes as a function of elapsed time since the start of injection. The traveltimes were calculated from the reservoir simulations using the Hill algorithm (19). The onset times are indicated by the unfilled squares.

depend upon the characteristics of the particular field site and the experimental setup. For example, we can use the pre-injection time series to estimate the noise-level.
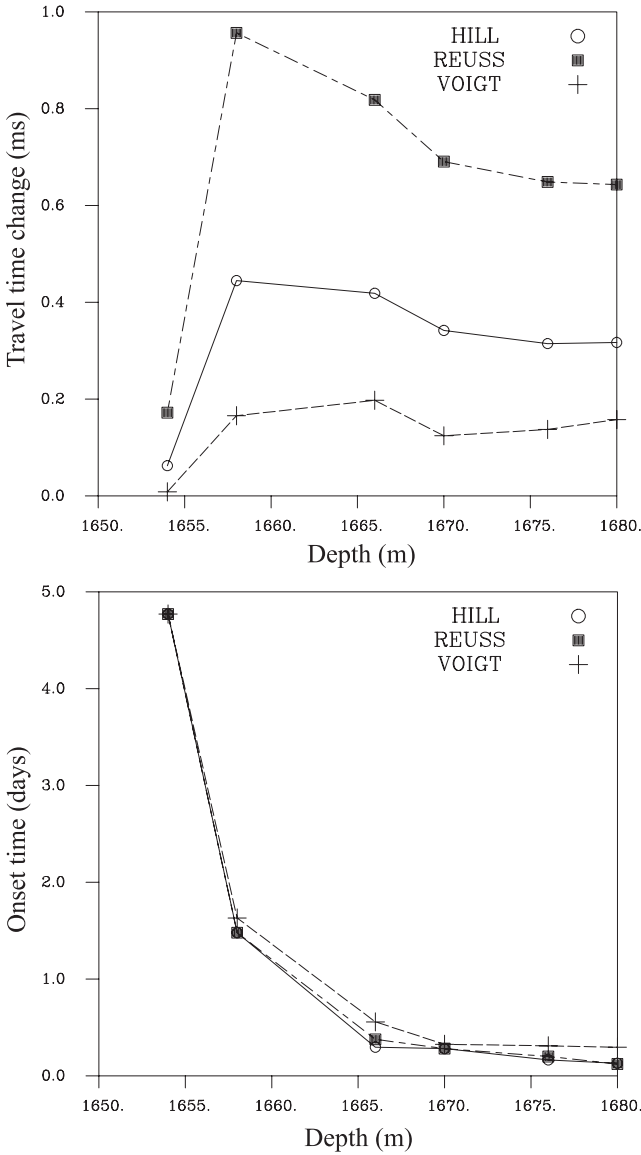
The changes in seismic traveltime for each of the six receivers are plotted in Fig. 6 as a function of the elapsed time since the start of injection. A value of zero in this plot indicates no deviation from the traveltime observed before the injection. For these calculations we use the approach of Hill (1963) in which the Voigt and Reuss bounds are averaged [see eq. (19)]. The somewhat discontinuous changes in the traveltime deviation are due to the 3 m grid spacing in the

flow model (Fig. 1). When the carbon dioxide enters a grid block the saturation in the entire grid block is changed by the simulator. Thus, the saturation of entire 3-m regions change abruptly in our reservoir simulation, leading to corresponding jumps in seismic velocity. A finer discretization would reduce these rapid changes, with a corresponding increase in computation time. The changes in traveltime for the four deepest receivers (1666, 1670, 1676 and 1680 m) occur first, at around 0.1 to 0.3 d. The early onset of a traveltime change at the deepest receivers is in accordance with our intuition, because these four ray paths intersect the reservoir layer nearest to the injector, some 10 to 15 m from the injection well (Fig. 5). For the receiver located at a depth of 1658 m in the observation well, the initial change in traveltime does not occur until about 1 d after the start of injection. The ray path for this receiver intersects the reservoir layer somewhere between 15 and 25 m from the injection well. The first notable changes in the traveltime to the shallowest receiver (1654 m) do not occur until around 4.5 d following the beginning of injection. The later onset time agrees with the fact that this raypath intersects the reservoir layer furthest from the injection site, at a distance of 30 m or more. Note also, that the magnitude of this traveltime change, less than 0.1 ms, is much smaller than the 0.3 to 0.4 ms changes found at the other receivers. An explanation for this smaller change in arrival time is that the ray path for this receiver has a much shorter component within the high permeability layer and thus encounters very little carbon dioxide along its travel path (Fig. 5).

Now consider how variations in the method used to compute the effective fluid bulk modulus influences the magnitude of the traveltime change and the onset time at each receiver. We use the Reuss (18) and Voigt (17) algorithms to map saturation changes into moduli and velocity changes used in the eikonal equation. The calculated traveltime changes following the start of carbon dioxide injection are plotted in Fig. 7. There are significant variations in the size of the traveltime changes, around a factor of five, between the Voigt and Reuss values. Note that the time at which significant

Figure 7. Deviations from pre-injection traveltimes as a function of elapsed time since the start of injection. (Left) The traveltimes were calculated from the reservoir simulations using the Reuss algorithm. (Right) The traveltimes were calculated from the reservoir simulations using the Voigt algorithm. The open squares denote the onset times at each source–receiver pair.

Figure 8. (Top) Peak traveltime change for each of the six receivers plotted at their respective depths. The three curves signify the three methods (Voight, Reuss, and Hill) for computing seismic velocities. (Bottom) Onset times for each receiver plotted at the depth of the instrument in the observation borehole.

changes are first observed at each receiver, the onset time, denoted by the unfilled squares in Fig. 7, does not change significantly when either the Reuss or Voigt approach is used. These observations are encapsulated in the two panels in Fig. 8. The upper panel displays the peak traveltime changes for the three approaches (Hill, Reuss and Voigt) for all receivers. The factor of five variation in magnitude is clear in this figure. The lower panel is a plot of the onset times for each set of estimates. The onset time does not vary significantly when the algorithm for computing the effective fluid bulk modulus is changed. The variations are roughly 0.1 to 0.2 d, which is less than 5 per cent of the peak value of the onset time, which is almost 5 d.

2.3 An iterative inversion algorithm for permeability

We now outline an algorithm for estimating permeability variations within a reservoir given a collection of onset times. The algorithm

is iterative in the sense that we start with a reservoir model and modify it in a succession of updates designed to better match the observed onset times. The onset times are derived from the seismic traveltime histories. Given sufficient ray coverage, one could conduct a sequence of seismic tomographic inversions to construct velocity histories for the grid blocks of the reservoir model. Then the onset time for each grid block may be derived from the velocity histories. For the synthetic case treated here (Fig. 5) we only have six observations for the seismic receivers. The onset times are computed from the traveltime changes (Fig. 6). We attribute the onset time to a saturation change in the reservoir grid blocks that the seismic ray traverses. It is assumed that the carbon dioxide propagates away from the injection point and that the propagation time of the carbon dioxide increases monotonically from the injector. Thus, we assume that earliest seismic traveltime change, in particular the onset time of the change, is due to saturation changes in the grid block of the reservoir model traversed by the ray path and nearest to the injection well. We construct the flow path from the center of this block back to the injector to obtain the path **X** used in the integral (16).

The basis for the inversion algorithm is a discrete version of eq. (16)

$$\Delta \tau_i = - \sum_{j=1}^{N} I_j \frac{\Delta l_{ij}}{K_j} \delta K_j, \qquad (28)$$

where $\Delta \tau_i$ denotes the change in saturation arrival time (onset time) for the ith observation, the sum is over the N grid blocks of the reservoir model, K_j is the background permeability of the jth grid block, δK_j is the permeability update for that grid block, and Δl_{ij} is the path length for the ith trajectory, $\mathbf{X}_i$, in the jth grid block. If the trajectory does not intersect a particular grid block then Δl_{ij} is zero and there is no contribution to the sum. For a given set of onset times, we will have a collection of equations, each in the form of the linear constraint (28). We may write the system of equations in matrix-vector form

$$\mathbf{d} = \mathbf{A} \delta \mathbf{K}, \qquad (29)$$

where the elements of **A** are given by

$$A_{ij} = -I_j \frac{\Delta l_{ij}}{K_j} = -\frac{1}{|\mathbf{v}_n|_j} \frac{\Delta l_{ij}}{K_j}, \qquad (30)$$

d is the vector of onset time residuals and $\delta \mathbf{K}$ is the vector containing the permeability update. At every iteration we seek updates that improve the match to the observed onset times or minimize the magnitude of the squared misfit vector

$$\Psi(\delta \mathbf{K}) = (\mathbf{d} - \mathbf{A} \delta \mathbf{K})^T (\mathbf{d} - \mathbf{A} \delta \mathbf{K}), \qquad (31)$$

possibly subject to additional regularization terms penalizing attributes of the model such as its spatial roughness or its vector norm (Menke 1989). The vector $\delta \mathbf{K}$ that minimizes (31) is obtained by solving the necessary equations for a minimum (Noble & Daniel 1977, p. 60)
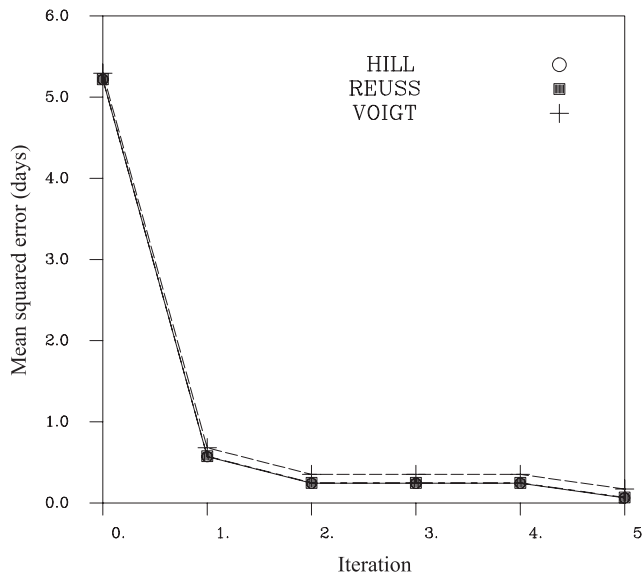
$$\mathbf{A}^T \mathbf{A} \delta \mathbf{K} = \mathbf{A}^T \mathbf{d}. \qquad (32)$$

We solve the linear system (32) using the iterative LSQR algorithm of Paige & Saunders (1982). For the mth iteration, the update is given by

$$\mathbf{K}_m = \mathbf{K}_{m-1} + \delta \mathbf{K}_m, \qquad (33)$$

and for each iteration we conduct a full reservoir simulation using the previous model $\mathbf{K}_{m-1}$ to compute the elements of the matrix **A** and the residuals.
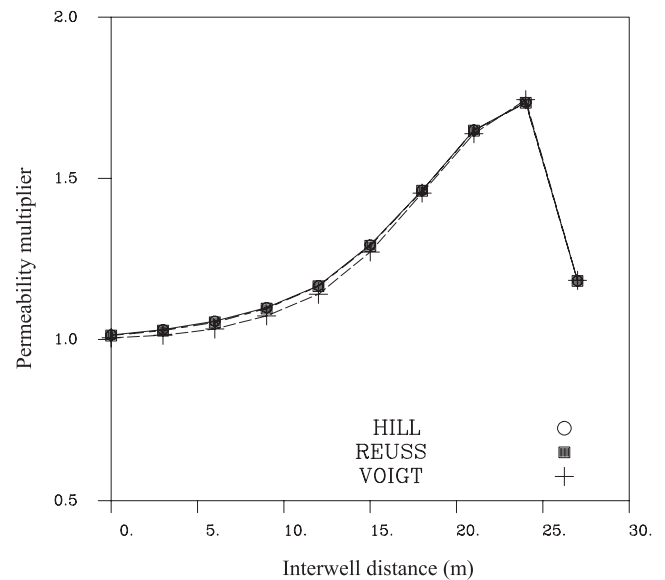
Figure 9. Mean squared error as a function of the number of iterations of the inversion algorithm. The three curves signify inversions for the Hill, Reuss, and Voigt onset times.

Figure 10. Estimated permeability variations between the injection and observation wells. Each curve is associated with a distinct inversion, based upon Hill, Reuss, and Voigt onset times.

Figure 11. Reference and estimated interwell permeability variations. Two reference permeability variations, one directly along the line between the two wells and one offset 3 m to the west of the line between the wells, in a higher permeability region.

To examine the impact of varying the method used to calculate the effective fluid bulk modulus, we consider inversions using the Hill, Reuss, and Voigt onset times (Fig. 8). The Hill algorithm is used to calculate the sensitivities and the residuals for each inversion. The synthetic onset times **d** are computed using the three approaches (Hill, Reuss, and Voigt). The resulting misfit reduction, as a function of the number of iterations, is essentially identical for the Hill and Reuss onset times (Fig. 9). For the Voigt onset times the final misfit is marginally larger but the total reduction is still almost two orders of magnitude and the final misfit is quite small.

In order to evaluate the impact of the different rock physics models on the inversion of onset times, we compare the three sets of permeability estimates, Voigt, Reuss, and Hill, with each other and with the reference permeability variation between the two boreholes. In Fig. 10, we plot the variation of the permeability in the reservoir layer between the wells for the inversions of the three sets of onset times. The position of this line within the reference model is plotted in Fig. 2. The agreement between the three estimates is good and each model indicates increasing permeability as the observation well is approached. This overall increase in permeability from the injection well to the observation well is also seen in the reference model (Fig. 2). A more detailed comparison is presented in Fig. 11 in which we plot the Hill permeability multiplier estimates along with those of the reference model. We plot two cross-sections through the reference model, one directly on the line between the two boreholes and a parallel cross-section offset 3 m to the west in a region of higher permeability. One of the difficulties associated with interpretating crosswell observations is the fact that fluid may flow out of the plane that is imaged by the seismic data. In the present case higher permeabilities to the west leads to significant fluid flow adjacent to the crosswell plane, leading to an apparent higher permeability. Thus, the permeability estimates follow the highest permeability values of the two cross-sections.
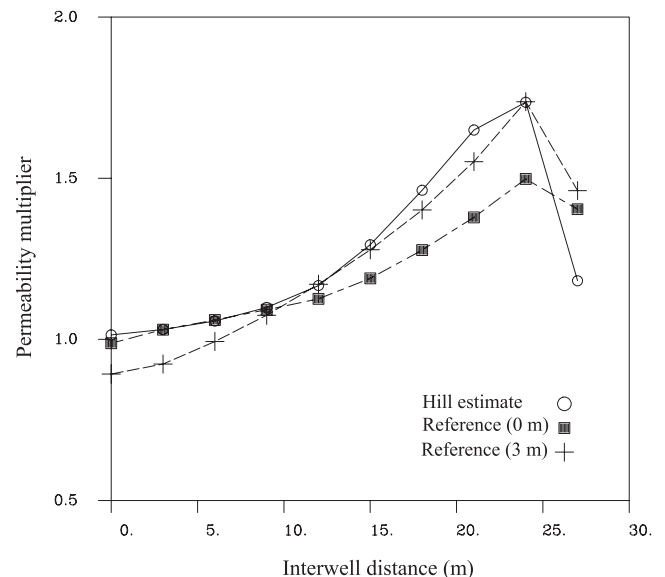
3 APPLICATION: CONTINUOUS ACTIVE SEISMIC SOURCE MONITORING (CASSM) OF THE INJECTION OF CARBON DIOXIDE AT THE FRIO SITE

3.1 Overview

The Frio I and II brine pilot experiments involved the monitoring of carbon dioxide injected into deep (1664 to 1666 m), high porosity, sand formations. The dipping sand layers flank a salt dome in the vicinity of Houston, Texas. Some 380 tons of carbon dioxide were injected over a period of 5 d at an average rate of 0.9 kg s^{-1}. The migration of the injected carbon dioxide was monitored by both crosswell seismic techniques and geochemical fluid sampling

(Freifeld *et al.* 2005; Daley *et al.* 2007). The arrival of the carbon dioxide at the monitoring well, some 2 d after the start of injection, was detected by continuous U-tube fluid sampling in the observation well (Daley *et al.* 2011).

The small-scale pilots were useful for calibrating models and techniques at intermediate length scales, somewhere between the core and log scale and the scale provided by surface seismic observations (Daley *et al.* 2011). The target formation for the Frio II pilot experiment was the 17 m thick fluvial Blue sand. The sediments in the area dip 18° from the observation well towards the injection well 30 m away (Daley *et al.* 2011). Logs taken in the injection well indicate variable permeabilities in the region of injection, with values as high as 4 Darcies in isolated locations and average porosities of 25 to 30 per cent. Of particular importance for the experiment was the existence of a 2–3 m sequence of generally high permeability layers intersecting the injection interval between 1663 and 1666 m in depth. Two permeability logs, obtained using distinct methods, indicate the presence of this zone but displayed different internal structure and also differ to some degree outside of this zone. The indirect estimates provided by the permeability logs were calibrated using core measurements. The resulting high permeabilities were later validated during pressure interference testing conducted in advance of the injection (Daley *et al.* 2011). A sonic log run in the injection well provided the background velocity model, which is identical to that used in the illustration presented earlier (Fig. 3). There is fair agreement between the observed and calculated pre-injection traveltimes at each of the six receivers.

3.2 CASSM observations

While the U-tube sampler provides an estimate of the large-scale fluid traveltime from the injector to the observation well, it does not reveal much about propagation of the carbon dioxide in the region between the wells. More details on the interwell propagation are provided by the Continuous active-source seismic monitoring (CASSM) system, designed and deployed at the Frio site by scientists from Lawrence Berkeley National Laboratory (Daley *et al.* 2008; Daley *et al.* 2011). The overall CASSM source-receiver geometry is indicated in Fig. 5. A single source, located above the formation, is used to propagate elastic waves to receivers in an adjacent borehole. Twenty-four hydrophone sensors were deployed but only 13 provided usable data due to electrical leakage. Of the 13 instruments, we use six which recorded elastic energy propagating through the formation and with sufficient signal-to-noise for the estimation of onset times (Fig. 12). The receivers above the high-permeability layer were not used to avoid the effects of possible density-driven vertical migration of carbon dioxide within the well itself. In particular Daley *et al.* (2011) note that one hydrophone, at a depth of 1650 m, had a significantly larger traveltime increase of over 1 ms. The waveform associated with this hydrophone changed dramatically during the injection, leading to difficulties in consistently identifying the onset time. Therefore, until we can better resolve the situation for the shallow hydrophones, we have decided to focus on receivers at or below the depth of the high-permeability layer. Due to interference with a downhole pressure gauge the recording was delayed until 2 hr after the start of injection. During its operation four pulses per second were recorded and stacked in 15 min intervals, for an effective 15 min sampling rate. The resulting deviations in traveltimes from their pre-injection values are plotted in Fig. 12.
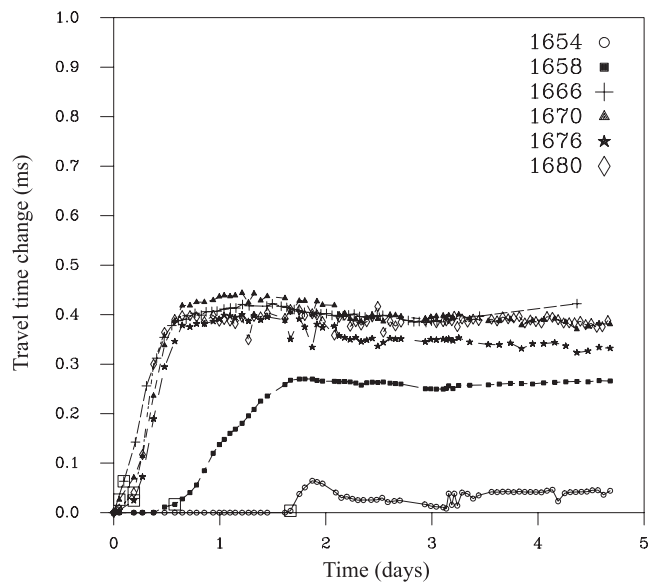

Figure 12. Observed traveltime changes as a function of the time since the start of injection. The six curves are associated with instruments at different depths in the observation well. The onset times are indicated by the open squares.

The general features of the traveltime changes in Fig. 12 are similar to those found in our numerical illustration (Fig. 6). In particular, the deeper receivers (1666, 1670, 1676 and 1680 m) cluster with early onset times while the shallower receivers (1658 and 1654 m) have successively larger onset time. The onset times are much shorter for the actual Frio observations. We found that this was a density effect, due to the dip of the formation and the fact that the carbon dioxide is less dense than the *in situ* saline water. This gravitational effect was not modelled in the numerical illustration but was included in modelling the actual Frio II experiment. Both the predicted traveltime changes based upon the Hill model and the observed traveltime changes (Fig. 12) increase rapidly around the onset time and quickly plateau to constant values. Finally, the magnitude of the traveltime change is much smaller at the shallowest receiver (1654 m). This is most likely due to the fact that receiver is situated near the top of the formation and the seismic energy does not propagate through the entire carbon dioxide saturated layer (see Fig. 5). A notable difference between the synthetic traveltime changes and the observed changes is the smaller magnitude of the observed traveltime change associated with the receiver at a depth of 1658 m. This may be due to a variation in the properties of the rock physics model mapping from saturation to seismic velocity. The sensitivity to the rock physics model may be seen by comparing the relative magnitudes of the Reuss and Voigt models in Fig. 7. Alternatively, it might be due to a thinning of the formation near the observation well or some other deviation from our reservoir modelling.

3.3 Onset times and estimates of permeability variations

From the traveltime histories in Fig. 12 we estimated the onset times, the calendar time at which the traveltime change exceeds 5 per cent of the peak change. We used a smaller value to compute the onset time because the signal-to-noise of the Frio CASSM data allowed for a lower threshold. Using the numerical reservoir model (Fig. 1) and the seismic velocity structure discussed earlier (Fig. 3), we set up the inverse problem. In particular, we define all the quantities needed

to completely specify the data and coefficients in eqs (29) and (30). Our initial reservoir model consists of a uniform layer 2.5 m thick with a porosity of 25 per cent and a horizontal permeability of $3.0 \times 10^{-12}\,\mathrm{m}^2$. The layer dips, as in the synthetic example, but we now account for the associated density effects. The relative permeability and capillary pressure behaviour were taken from earlier studies (Doughty *et al.* 2008; Daley *et al.* 2011). The approach of Hill (Hill 1963) was used to relate the saturation changes to velocity changes in the poroelastic model. For each iteration of the inversion algorithm, the trajectories and related sensitivities are based on the results of a reservoir simulation with updated reservoir properties. The final misfit obtained after three iterations, around 0.1 d, is similar to that obtained in the synthetic test. The final model of permeability variation between the wells is plotted in Fig. 13. There are generally higher permeabilities in the region between the wells. The drop off in permeability near the monitoring well is probably an artifact of poor sampling at that end. In Fig. 13 we have also plotted the all the ray paths from the start of injection until the onset time at each receiver. The variation in ray paths in Fig. 13 allows us to examine any deviations from the assumption that the propagation does not change between the start of injection and the onset time. In general this appears to be true for the source–receiver pairs used here. However, for two source–receiver pairs we observe some variation in ray paths. Given the 3 m discretization of the
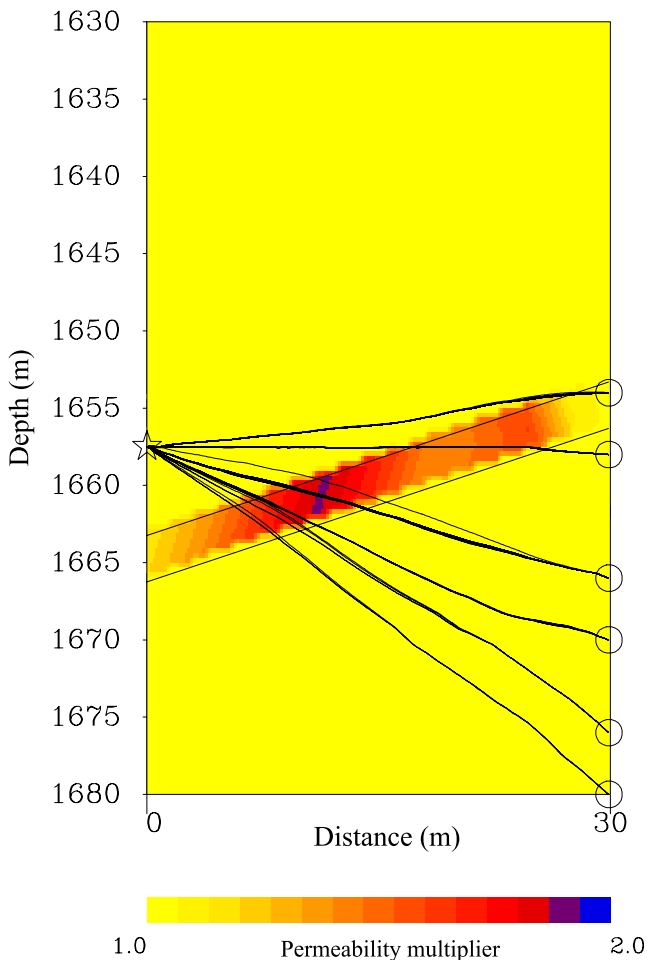
permeability in the layer, the variations are probably not significant. We should note that the deviations in the ray paths following the onset times are much larger and thus should be taken into account when considering later traveltime changes.

The initial and final calculated traveltime histories are shown in Fig. 14. The final calculated onset times are in fair agreement with the observed values, as indicated in Fig. 15. For example, the final onset time at the shallowest receiver (1654 m) is slightly less then 2 d. The arrival time is compatible with the carbon dioxide breakthrough time obtained from the U-tube sampler (Daley *et al.* 2011). The onset time for the receiver at 1658 m depth has also advanced in time to about 0.7 d, in better agreement with the observed value. Even though the magnitudes are not matched, there is qualitative agreement between the final predicted and the actual observed traveltime changes.

4 CONCLUSIONS

Relating changes in reservoir properties to changes in geophysical observations can be a difficult task, often complicated by the fact that time-lapse changes are typically severely under-sampled in time. Thus, temporal changes are almost always aliased and distinct processes, such as fluid pressure changes and saturation changes can be confused. Such a confounding of signals can occur even though these processes operate on distinctly different time scales. For example, at the Frio site transient pressure changes can propagate between the wells in less then a minute while saturation changes may take more than a day to travel the same distance. This points to the importance of adequate temporal sampling to better understand fluid flow in the subsurface. With sufficient sampling in time, it is possible to estimate the onset of a change in seismic arrival time for a given source–receiver pair. Such onset times have a rather direct relationship to flow-related changes in the state of a reservoir. For example, at the Frio site the initiation of changes in seismic arrival times is related to fluid saturation breakthrough times. Onset times are less influenced by the rock physics model relating fluid saturation changes to changes in seismic velocity. For this reason, onset times provide a robust basis for reservoir characterization based upon geophysical observations.

As the development of the CASSM system indicates (Ajo-Franklin *et al.* 2011), it is certainly possible to improve the temporal sampling associated with the geophysical monitoring of flow processes. Improvements in temporal sampling are also on the horizon for time-lapse seismic reflection monitoring (Bakulin *et al.* 2012). It is hoped that these enhancements can continue in better constrained settings, such as full crosswell and surface seismic reflection surveys. The approach described in this paper can be a tool for data reduction, allowing for the extraction of a 3-D field of onset times from a 4-D time lapse data set. Finally, onset times also provide a means for combining multiple geophysical data sets, such as seismic and ground penetrating radar observations. Such combinations of data can better constrain reservoir geometry (Doetsch *et al.* 2010b) and may be combined with hydrological data for improved aquifer characterization (Lochbuhler *et al.* 2013).

Figure 13. Estimated permeability variations between the injection and observation wells based upon the inversion of data from the Frio II pilot experiment. The ray paths for the six receivers and for all times up to the onset time are also plotted here.

ACKNOWLEDGEMENTS
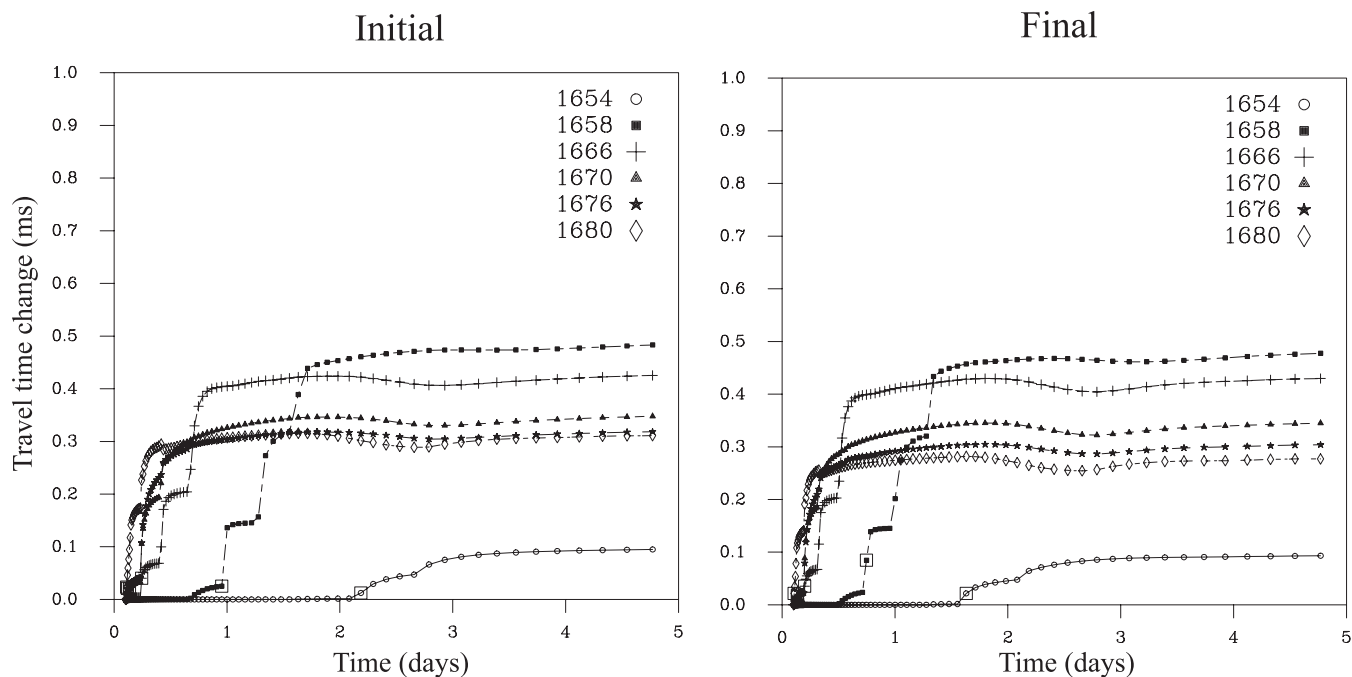
Initial

Final

Figure 14. Traveltime histories calculated using the initial and final reservoir models of the iterative inversion algorithm.
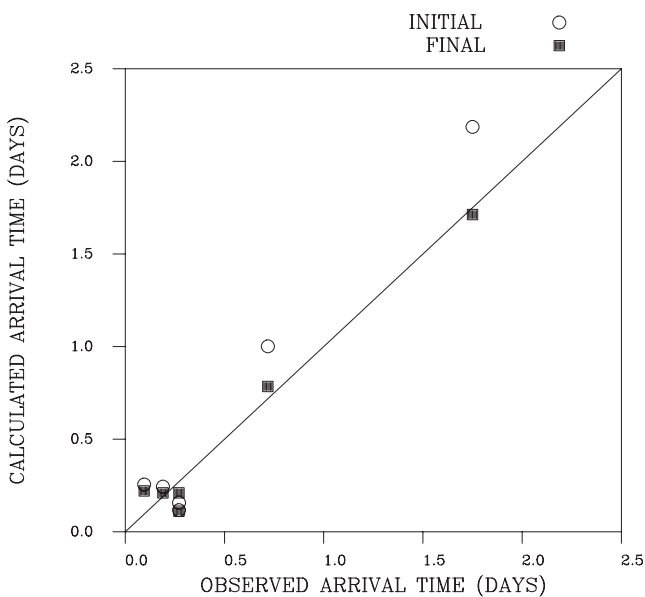
Figure 15. Plot of the initial fit to the observed onset times (open circles) and the final fit (filled squares) based upon the permeability model plotted in Fig. 13. For an ideal fit the points would lie upon the 45° line plotted in the figure.

Secretary for Fossil Energy, Office of Coal and Power Systems, through the National Energy Technology Laboratory of the US Department of Energy.

REFERENCES

Ajo-Franklin, J., Daley, T., Butler-Veytia, B., Peterson, J., Wu, Y., Kelly, B. & Hubbard, S., 2011. Multi-level continuous active source seismic monitoring (ML-CASSM): mapping shallow hydrofracture evolution at a TCE contaminated site, *SEG Expanded Abstracts,* **30,** 3727, doi:10.1190/1.3627980.

Amelung, F., Galloway, D.L., Bell, J.W., Zebher, H.A. & Laczniak, R.J., 1999. Sensing the ups and downs of Las Vegas – InSAR reveals structural control of land subsidence and aquifer-system deformation, *Geology,* **27,** 483–486.

Arts, R., Eiken, O., Chadwick, A., Zweigel, P., van der Meer, L. & Zinszner, B., 2004. Monitoring of CO_2 injected at Sleipner using time-lapse seismic data, *Energy,* **29,** 1383–1392.

Bakulin, A., Burnstad, R., Jervis, M. & Kelamis, P., 2012. Evaluating permanent seismic monitoring with shallow buried sensors in a desert environment, *SEG Technical Program Expanded Abstracts,* Las Vegas, 1–5.

Behrens, R., Condon, P., Haworth, W., Bergeron, M., Wang, Z. & Ecker, C., 2002. Monitoring of water influx at Bay Marchand: the practical use of 4D in an imperfect world, *SPE Res. Eval. Eng.,* **5**(5), 410–420.

Benson, R.D. & Davis, T.L., 2000. Time-lapse seismic monitoring and dynamic reservoir characterization, Central Vacuum Unit, Lea County, New Mexico, *SPE Res. Eval. Eng.,* **3,** 88–97.

Burkhart, T., Hoover, A.R. & Flemings, P.B., 2000. Time-lapse (4D) seismic monitoring of primary production of turbidite reservoirs as South Timbalier Block 295, offshore Louisiana, Gulf of Mexico, *Geophysics,* **65,** 351–367.

Camporese, M., Cassiani, G., Deiana, R. & Salandin, P., 2011. Assessment of local hydraulic properties from electrical resistivity tomography monitoring of a three-dimensional synthetic tracer test experiment, *Water Resour. Res.,* **47,** W12508, doi:10.1029/2011WR010528.

Castillo, W., Hunter, S., Harben, P., Wright, C., Conant, R. & Davis, E., 1997. Deep hydraulic fracture imaging: recent advances in tiltmeter technologies, *Int. J. Rock. Mech. Min. Sci.,* **34,** 3–4.

Chadwick, R.A., Williams, G.A., Williams, J.D.O. & Noy, D.J., 2012. Measuring pressure performance of a large saline aquifer during industrial-scale CO_2 injection: the Utsira Sand, Norwegian North Sea, *Int. J. Greenhouse Gas Cont.,* **10,** 374–388.

Chapman, C.H., 2004. *Fundamentals of Seismic Wave Propagation,* Cambridge Univ. Press.

Coscia, I., Greenhalgh, S., Linde, N., Doetsch, J., Marescot, M., Gunther, T., Vogt, T. & Green, A.G., 2011. 3D crosshole ERT for aquifer characterization and monitoring of infiltrating river water, *Geophysics,* **76,** G49–G59.

Coscia, I., Linde, N., Greenhalgh, S., Vogt, T. & Green, A., 2012. Estimating traveltimes and groundwater flow patterns using 3D time-lapse crosshole

ERT imaging of electrical resistivity fluctuations induced by infiltrating river water, *Geophysics,* **77,** E239–E250.

Daley, T.M., Solbau, R.D., Ajo-Franklin, J.B. & Benson, S.M., 2007. Continuous active-source monitoring of CO_2 injection in a brine aquifer, *Geophysics,* **72,** A57–A61.

Daley, T.M., Myer, L.R., Peterson, J.E., Majer, E.L. & Hoversten, G.M., 2008. Time-lapse crosswell seismic and VSP monitoring of injected CO_2 in a brine aquifer, *Environ. Geol.,* **54,** 1657–1665.

Daley, T.M., Ajo-Franklin, J.B. & Doughty, C., 2011. Constraining the reservoir model of an injected CO_2 plume with crosswell CASSM at the Frio-II brine pilot, *Int. J. Greenhouse. Gas Cont.,* **5,** 1022–1030.

Day-Lewis, F., Harris, J.M. & Gorelick, S.M., 2002. Time-lapse inversion of cross-well radar data, *Geophysics,* **67,** 1740–1752.

Doetsch, J., Linde, N. & Binley, A., 2010a. Structural joint inversion of time-lapse crosshole ERT and GPR traveltime data, *Geophys. Res. Lett.,* **37,** L24404, doi:10.1029/2010GL045482.

Doetsch, J., Linde, N., Coscia, I., Greenhalgh, S.A. & Green, A.G., 2010b. Zonation for 3D aquifer characterization based on joint inversions of multimethod crosshole geophysical data, *Geophysics,* **75,** G53–G64.

Doughty, C., Freifeld, B.M. & Trautz, R.C., 2008. Site characterization for CO_2 geologic storage and vice versa: the Frio brine pilot, Texas, USA as a case study, *Environ. Geol.,* **54,** 1635–1656.

Du, J. & Olson, J.E., 2001. A poroelastic reservoir model for predicting subsidence and mapping subsurface pressure fronts, *J. Petrol. Sci. Eng.,* **30,** 181–197.

Eastwood, J., Lebel, J.P., Dilay, A. & Blakeslee, S., 1994. Seismic monitoring of steam-based recovery of bitumen, *Leading Edge,* **4,** 242–251.

Evans, K.F., Holzhausen, G.R. & Wood, M.D., 1982. The geometry of a large-scale nitrogen gas hydraulic fracture formed in Devonian shale: an example of fracture mapping using tiltmeters, *Soc. Petrol. Eng. J.,* **22,** 755–763.

Fielding, E.J., Blom, R.G. & Goldstein, R.M., 1998. Rapid subsidence over oil fields measured by SAR interferometry, *Geophys. Res. Lett.,* **25,** 3215–3218.

Freifeld, B.M., Trautz, R.C., Kharaka, Y.K., Phelps, T.J., Myer, L.R., Hovorka, S.D. & Collins, D.J., 2005. The U-tube: a novel system for acquiring borehole fluid samples from a deep geologic CO_2 sequestration experiment, *J. geophys. Res.,* **110,** B10203, doi:10.1029/2005JB003735.

Gassmann, F., 1951. Ueber die elastizitat poroser medien, *Vier. Der. Natur., Heft,* **96,** 1–23.

Ghosh, R. & Sen, M.K., 2012. Predicting subsurface CO_2 movement: from laboratory to field scale, *Geophysics,* **77,** M27–M37.

Gosselin, O. *et al.,* 2003. History matching using time-lapse seismic (HUTS), *SPE Paper,* 84464, doi:10.2118/84464-MS.

Greaves, R.J. & Fulp, T., 1987. Three dimensional seismic monitoring of an enhanced oil recovery process, *Geophysics,* **52,** 1175–1187.

Guilbot, J. & Brackin, S., 2002. 4-D constrained depth conversion for reservoir compaction estimation: application to Ekofisk field, *Leading Edge,* **21,** 302–308.

Hashin, Z. & Shtrikman, S., 1963. A variation approach to the elastic behavior of multiphase materials, *J. Mech. Phys. Solids,* **11,** 127–140.

He, W., Guerin, G., Anderson, R.N. & Mello, U.T., 1998. Time-dependent reservoir characterization of the LF sand in the South Eugene Island 330 Field, Gulf of Mexico, *Leading Edge,* **17,** 1434–1438.

Hill, R., 1963. Elastic properties of reinforced solids: some theoretical principles, *J. Mech. Phys. Solids,* **11,** 357–372.

Hodgson, N., MacBeth, C., Duranti, L., Rickett, J. & Nihei, K., 2007. Inverting for reservoir pressure change using time-lapse time strain: application to the Genesis field, Gulf of Mexico, *Leading Edge,* **26,** 649–652.

Hoversten, G.M., Gritto, R., Washbourne, J. & Daley, T., 2003. Pressure and fluid saturation prediction in a multicomponent reservoir using combined seismic and electromagnetic imaging, *Geophysics,* **68,** 1580–1591.

Huang, X., Meister, L. & Workman, R., 1998. Improving production history matching using time-lapse seismic data, *Leading Edge,* **17,** 1430–1433.

Jandani, A. *et al.,* 2009. Reconstruction of the water table from self-potential data: a Bayesian approach, *Groundwater,* **47,** 213–227.

Johnson, D.L., 2001. Theory of frequency dependent acoustics in patchy saturated porous media, *J. acoust. Soc. Am.,* **110,** 682–694.

Johnston, D.H., McKenny, R.S., Verbeek, J. & Almond, J., 1998. Time-lapse seismic analysis of Fulmar Field, *Leading Edge,* **17,** 1420–1428.

Karaoulis, M., Revil, A., Werkema, D.D., Minsley, B., Woodruff, W.F. & Kemna, A., 2011. Time-lapse 3D inversion of complex conductivity data using an active time constrained (ATC) approach, *Geophys. J. Int.,* **187,** 237–251.

Kowalsky, M.B., Finsterle, S. & Rubin, Y., 2004. Estimating flow parameter distributions using ground-penetrating radar and hydrological measurements during transient flow in the vadose zone, *Adv. Water Resour.,* **27,** 583–599.

Kowalsky, M.B., Chen, J. & Hubbard, S., 2006. Joint inversion of geophysical and hydrological data for improved subsurface characterization, *Leading Edge,* **25,** 730–734.

LaBrecque, D.J. & Yang, X., 2001. Difference inversion of ERT data: a fast inversion method for 3-D in situ monitoring, *J. Environ. Eng. Geophys.,* **6,** 83–89.

Landa, J.L. & Horne, R.N., 1997. A procedure to integrate well test data, reservoir performance history, and 4-D seismic information into a reservoir description, in *Proceedings of the SPE Annual Technical Conference and Exhibition,* October 5–8, San Antonio, Texas.

Landro, M., 2001. Discrimination between pressure and fluid saturation changes from time-lapse seismic data, *Geophysics,* **66,** 836–844.

Lazaratos, S.K. & Marion, B.P., 1997. Crosswell seismic imaging of reservoir changes caused by CO_2 injection, *Leading Edge,* **16,** 1300–1307.

Lee, D.S., Stevenson, V.M., Johnston, P.F. & Mullen, C.E., 1995, Time-lapse crosswell seismic tomography to characterize flow structure in the reservoir during thermal stimulation, *Geophysics,* **60,** 660–666.

Lochbuhler, T., Doetsch, J., Brauchler, R. & Linde, N., 2013. Structure-coupled joint inversion of geophysical and hydrological data, *Geophysics,* **78,** ID1–ID14.

MacBeth, C. & Al-Maskeri, Y., 2006. Extraction of permeability from time-lapse seismic data, *Geophys. Prospect.,* **54,** 333–349.

Martinez-Pagan, P., Jardani, A., Revil, A. & Haas, A., 2010. Self-potential monitoring of a salt plume, *Geophys. J. Int.,* **75,** WA17–WA25.

Mathisen, M.E., Vasiliou, A.A., Cunningham, P., Shaw, J., Justice, J.H. & Guinzy, N.J., 1995. Time-lapse crosswell seismic tomogram interpretation: implications for heavy oil reservoir characterization, thermal recovery process monitoring, and tomographic imaging technology, *Geophysics,* **60,** 631–650.

Mavko, G., Mukerji, T. & Dvorkin, J., 1998. *The Rock Physics Handbook,* Cambridge Univ. Press.

McKenna, J., Sherlock, D. & Evans, B., 2001. Time-lapse 3-D seismic imaging of shallow subsurface contaminant flow, *J. Contam. Hydrol.,* **53,** 133–150.

Menke, W., 1989. *Geophysical Data Analysis: Discrete Inverse Theory,* Academic Press.

Miller, C.R., Routh, P.S., Brosten, T.R. & McNamara, J.P., 2008. Application of time-lapse ERT to watershed characterization, *Geophysics,* **73,** G7-G17.

Mossop, A. & Segall, P., 1999. Volume strain within the Geysers geothermal field, *J. geophys. Res.,* **104,** 29113–29131.

Müller, T.M., Gurevich, B. & Lebedev, M., 2010. Seismic wave attenuation and dispersion resulting from wave-induced flow in porous rocks—a review, *Geophysics,* **75,** A147–A164.

Noble, B. & Daniel, J.W., 1977. *Applied Linear Algebra,* Prentice-Hall.

Oppliger, G., Coolbaugh, M. & Shevenell, L., 2006. Improved visualization of satellite radar InSAR observed structural controls at producing geothermal fields using modeled horizontal surface displacements, *Geotherm. Res. Coun. Trans.,* **30,** 927–930.

Osdal, B., Husby, O., Aronsen, H.A., Chan, N. & Alsos, T., 2006. Mapping the fluid front and pressure buildup using 4D data on Norne Field, *Leading Edge,* **25,** 1134–1141.

Paige, C.C. & Saunders, M.A., 1982. LSQR: An algorithm for sparse linear equations and sparse least squares, *ACM Trans. Math. Software,* **8,** 43–71.

Palmer, I.D., 1990. Uplifts and tilts at Earth's surface induced by pressure transients from hydraulic fractures, *Soc. Petrol. Eng. Product. Eng.,* **5,** 324–332.

Peaceman, D.W., 1977. *Fundamentals of Numerical Reservoir Simulation,* Elsevier Scientific Publishing.

Podvin, P. & Lecomte, I., 1991. Finite difference computation of traveltimes in very contrasted velocity models: a massively parallel approach and its associated tools, *Geophys. J. Int.,* **105,** 271–284.

Pride, S.R., Berryman, J.G. & Harris, J.M., 2004. Seismic attenuation due to wave-induced flow, *J. geophys. Res.,* **109,** B01201, doi:10.1029/2003JB002639.

Pruess, K., 2004. The TOUGH Codes—a family of simulation tools for multiphase flow and transport processes in permeable media, *Vadose Zone J.,* **3,** 738–746.

Pruess, K., Oldenburg, C. & Moridis, G., 1999. *TOUGH2 User's Guide, Version 2.0,* LBNL Report, **43134,** Berkeley, 1999.

Rucci, A., Vasco, D.W. & Novali, F., 2010. Fluid pressure arrival time tomography: estimation and assessment in the presence of inequality constraints, with an application to production at the Krechba field, Algeria, *Geophysics,* **75,** O39–O55.

Rucci, A., Vasco, D.W. & Novali, F., 2013. Monitoring the geological storage of carbon dioxide using multicomponent SAR interferometry, *Geophys. J. Int.,* **193,** 197–208.

Schmidt, D.A. & Burgmann, R., 2003. Time-dependent land uplift and subsidence in the Santa Clara valley, California, from a large interferometric synthetic aperture radar data set, *J. geophys. Res.,* **108,** doi:10.1029/20002JB002267.

Shapiro, S.A., Audigane, P. & Royer, J.-J., 1999. Large-scale in situ permeability tensor from induced microseismicity, *Geophys. J. Int.,* **137,** 207–213.

Shapiro, S.A., Rothert, E., Rath, V. & Rindschwentner, J., 2002. Characterization of fluid transport properties of reservoirs using induced microseismicity, *Geophysics,* **67,** 212–220.

Shi, J.-Q., Xue, Z. & Durucan, S., 2007. Seismic monitoring and modelling of supercritical CO_2 injection into a water-saturated sandstone: interpretation of P-wave velocity data, *Int. J. Greenhouse Gas Cont.,* **1,** 473–480.

Smith, P., Berg, J.I., Eidsvig, S., Magnus, I., Verhelst, F. & Helgesen, J., 2001. 4-D seismic in a complex fluvial reservoir: The Snorre feasibility study, *Leading Edge,* **20,** 270–276.

Stancliffe, R.P.W. & van der Kooij, M.W.A., 2001. The use of satellite-based radar interferometry to monitor production activity at the Cold Lake heavy oil field, Alberta, Canada, *Am. Assoc. Petrol. Geol. Bull.,* **85,** 781–793.

Teatini, P. *et al.*, 2011. Geomechanical response to seasonal gas storage in depleted reservoirs: A case study in the Po River basin, Italy, *J. geophys. Res.,* **116,** 1–21.

Tong, F., Jing, L. & Zimmerman, R.W., 2009. An effective thermal conductivity model of geological porous material for coupled thermo-hydro-mechanical systems with multiphase flow, *Int. J. Rock Mech. Mining Sci.,* **46,** 1358–1369.

Tura, A. & Lumley, D.E., 1998. Subsurface fluid-flow properties from time-lapse elastic-wave reflection data, in *Proceedings of 43rd SPIE Annual Meeting,* July 19, San Diego, CA, 125–138.

Vasco, D.W., 2004a, Seismic imaging of reservoir properties: Time-lapse pressure changes, *Geophysics,* **69,** 511–521.

Vasco, D.W., 2004b. Estimation of flow properties using surface deformation and head data: A trajectory-based approach, *Water Resour. Res.,* **40,** W10104, doi:10.1029/2004WR003272, 1–14.

Vasco, D.W., 2011. On the propagation of a coupled saturation and pressure front, *Water Resour. Res.,* **47,** 1–21.

Vasco, D.W. & Datta-Gupta, A., 1999. Asymptotic solutions for solute transport: A formalism for tracer tomography, *Water Resour. Res.,* **35,** 1–16.

Vasco, D.W. & Datta-Gupta, A., 2001. Asymptotics, saturation fronts, and high resolution reservoir characterization, *Transport Porous Med.,* **42,** 315–350.

Vasco, D.W. & Ferretti, A., 2005. On the use of quasi-static deformation to understand reservoir fluid flow, *Geophysics,* **70,** O13–O27.

Vasco, D.W. & Finsterle, S., 2004. Numerical trajectory calculations for the efficient inversion of transient flow and tracer observations, *Water Resour. Res.,* **40,** 1–17.

Vasco, D.W., Yoon, S. & Datta-Gupta, A., 1999. Integrating dynamic data into high-resolution reservoir models using streamline-based analytic sensitivity coefficients, *Soc. Petrol. Eng. J.,* **4**(4), 389–399.

Vasco, D.W., Karasaki, K. & Doughty, C., 2000. Using surface deformation to image reservoir dynamics, *Geophysics,* **65,** 132–147.

Vasco, D.W., Karasaki, K. & Kishida, K., 2001. A coupled inversion of pressure and surface displacement, *Water Resour. Res.,* **37,** 3071–3089.

Vasco, D.W., Karasaki, K. & Nakagome, O., 2002. Monitoring production using surface deformation: the Hijiori test site and the Okuaizu geothermal field, Japan, *Geothermics,* **31,** 303–342.

Vasco, D.W., Datta-Gupta, A., Behrens, R., Condon, P. & Rickett, J., 2004. Seismic imaging of reservoir flow properties: Time-lapse amplitude changes, *Geophysics,* **69**(6), 1425–1442.

Vasco, D.W., Rucci, A., Ferretti, A., Novali, F., Bissell, R., Ringrose, P., Mathieson, A. & Wright, I., 2010. Satellite-based measurements of surface deformation reveal fluid flow associated with the geological storage of carbon dioxide, *Geophys. Res. Lett.,* **37,** doi:10.1029/2009GL041544, 1–5.

Vidale, J., 1988. Finite-difference calculation of travel times, *Bull. seism. Soc. Am.,* **78,** 2062–2076.

Wang, Z., Cates, M.E. & Langan, R.T., 1998. Seismic monitoring of a CO_2 flood in carbonate reservoir: a rock physics study, *Geophysics,* **63,** 1604–1617.

Watts, G.F.T., Jizba, D., Gawith, D.E. & Gutteridge, P., 1996. Reservoir monitoring of the Magnus field through 4D time-lapse seismic analysis, *Petrol. Geosci.,* **2,** 361–372.

White, J.E., 1975. Computed seismic speeds and attenuation in rocks with partial gas saturation, *Geophysics,* **40,** 224–232.

Wiener, O., 1910. Zur theorie der refraktionskonstanten, *Berichteuber Verhandlungen Koniglich-Sachsischen Gesellschaften Wisseschaften Leipzig,* **62,** 256–277.

Wright, C.A., 1998. Tiltmeter fracture mapping: from the surface and now downhole, *Petrol. Eng. Int.,* January, 50–63.

Wright, C.A., Davis, E.J., Minner, W.A., Ward, J.F., Weijers, L., Schell, E.J. & Hunter, S.P., 1998. Surface tiltmeter fracture mapping reaches new depths - 10,000 feet and beyond?, *Soc. Petrol. Eng.,* April, **39919,** doi:10.2118/39919-MS.

Zhang, F., Juhlin, C., Cosma, C., Tryggvason, A. & Pratt, R.G., 2012. Cross-well seismic waveform tomography for monitoring CO_2 injection: a case study from the Ketzin Site, Germany, *Geophys. J. Int.,* **189,** 629–646.

Zhang, J., Revil, A., Karaoulis, M. & Vasco, D., 2014. Crosswell 4D resistivity tomography localized the oil water encroachment front during water flooding, *Geophysics,* in press.

APPENDIX A

In this Appendix, we follow Peaceman (1977, p. 19) and derive the relationship between the velocity of the non-aqueous phase ($\mathbf{v}_n$) and the total velocity ($\mathbf{v}_t$), which is defined as

$$\mathbf{v}_t = \mathbf{v}_w + \mathbf{v}_n. \tag{A1}$$

From the definition of capillary pressure, eq. (2), we have

$$\nabla p_c = \nabla p_n - \nabla p_w. \tag{A2}$$

If we define the phase mobilities

$$\lambda_w = \frac{K k_{rw}}{\mu_w} \tag{A3}$$

and

$$\lambda_n = \frac{K k_{rn}}{\mu_n}, \tag{A4}$$

we can write the fluid phase velocities as

$$\mathbf{v}_w = -\lambda_w \left(\nabla p_w - \rho_w g \mathbf{Z} \right) \tag{A5}$$

$$\mathbf{v}_n = -\lambda_n \left(\nabla p_n - \rho_n g \mathbf{Z} \right). \tag{A6}$$

Rearranging and combining eqs (A2), (A5) and (A6) gives

$$(\lambda_n + \lambda_w)\mathbf{v}_n = \lambda_n \mathbf{v}_t - \lambda_n \lambda_w \left[\nabla p_c + (\rho_w - \rho_n)g\mathbf{Z}\right] \qquad \text{(A7)}$$

if we use eq. (A1) to eliminate $\mathbf{v}_w$. Dividing through by $\lambda_n + \lambda_w$ and defining the fractional flow function for the non-aqueous phase

$$f_n = \frac{\lambda_n}{\lambda_n + \lambda_w} \qquad \text{(A8)}$$

we can write (A7) as

$$\mathbf{v}_n = f_n \mathbf{v}_t - \lambda_w f_n \left[\nabla p_c + (\rho_w - \rho_n)g\mathbf{Z}\right]. \qquad \text{(A9)}$$

Treating the capillary pressure as a function of S_n we can write (A9) as

$$\mathbf{v}_n = f_n \mathbf{v}_t - \lambda_w f_n \left[\frac{dp_c}{dS_n}\nabla S_n + (\rho_w - \rho_n)g\mathbf{Z}\right], \qquad \text{(A10)}$$

and so relate the velocity of the non-aqueous phase to the fractional flow function f_n, the total fluid velocity, the capillary pressure, the saturation S_n, and the density difference of the two fluids.